Journal of Zhejiang University-SCIENCE A 2025 26(10):931-949
www.jzus.zju.edu.cn; www.springer.com/journal/11582
E-mail: jzus_a@zju.edu.cn

Research Article
https://doi.org/10.1631/jzus.A2500001

Effect of adjacent excavation on the mechanical response of proximal soil and tunnels in normally consolidated clay: centrifuge model testing and numerical simulation

Ren-Peng CHEN[1,2,3,4], Yong XU[1], Han-Lin WANG[2,3,4]✉, Fan-Yan MENG[2,3,4]

[1]*Institute of Geotechnical Engineering, College of Civil Engineering and Architecture, Zhejiang University, Hangzhou 310058, China*
[2]*College of Civil Engineering, Hunan University, Changsha 410082, China*
[3]*Hunan Provincial Engineering Research Center of Advanced Technology and Intelligent Equipment for Underground Space Development, Changsha 410082, China*
[4]*Key Laboratory of Building Safety and Energy Efficiency of the Ministry of Education, Changsha 410082, China*

Abstract: Urban spaces are becoming increasingly congested, and excavations are frequently performed close to existing underground structures such as tunnels. Understanding the mechanical response of proximal soil and tunnels to these excavations is important for efficient and safe underground construction. However, previous investigations of this issue have predominantly made assumptions of plane-strain conditions and normal gravity states, and focused on the performance of tunnels affected by excavation and unloading in sandy strata. In this study, a 3D centrifuge model test is conducted to investigate the influence of excavation on an adjacent existing tunnel in normally consolidated clay. The testing results indicate that the excavation has a significant impact on the horizontal deformation of the retaining wall and tunnel. Moreover, the settlements of the ground surface and the tunnel are mainly affected by the long-term period after excavation. The excavation is found to induce ground movement towards the pit, resulting in prolonged fluctuations in pore water pressure and lateral earth pressure. The testing results are compared with numerical simulations, achieving consistency. A numerical parametric study on the tunnel location shows that when the tunnel is closer to the retaining wall, the decreases in lateral earth pressure and pore water pressure during excavation are more pronounced.

Key words: Centrifuge model; Adjacent excavation; Tunnel; Retaining wall; Normally consolidated clay

1 Introduction

With continuous population growth and urbanization in China, urban underground development has involved an increasing number of adjacent projects. In construction, the design of a foundation pit must account for both environmental impact on the foundation pit and the influence of construction on existing underground structures, necessitating measures that prevent deformation and ensure safety (Hsieh and Ou, 1998; Ou and Hsieh, 2011; Shi JW et al., 2015a; Shi CH et al., 2016; Zhang DM et al., 2020; Meng et al., 2021; Ran et al., 2023; Sun et al., 2025; Zhang XH et al., 2025). Meanwhile, clay stratum is the primary ground material in numerous coastal areas, such as Shanghai, Singapore, and Ningbo (Sharma et al., 2001; Chen et al., 2016, 2021). The geological attributes of soft clay, which include a large void ratio, high compressibility, low strength, and low permeability, pose challenges to geotechnical engineering projects (Tan and Wei, 2012; Wang et al., 2018, 2024; Wang and Yin, 2020; Li et al., 2021; Peng et al., 2022). Considering these two issues, it is imperative to implement measures that mitigate the risk of structural failure and reduce economic losses.

To date, numerous studies have examined the impact of foundation pit excavation on adjacent existing tunnels. Developed methods have included on-site construction monitoring (Shi JW et al., 2015a; Liu GB et al., 2016; Shi CH et al., 2016; Liu Y et al., 2019), finite element numerical simulation (Ou et al., 1996; Ng et al., 2015a, 2015b; Shi, 2015; Shi et al., 2015b; Zheng et al.,

✉ Han-Lin WANG, wanghanlin@hnu.edu.cn
Han-Lin WANG, https://orcid.org/0000-0002-5416-9392

Received Jan. 3, 2025; Revision accepted Feb. 2, 2025;
Crosschecked Aug. 25, 2025

2017; Gao et al., 2024), theoretical analysis (Sagaseta, 1987; Liao et al., 2008; Zhang et al., 2015; Shi et al., 2017; Cheng et al., 2020), and physical model tests (Liang et al., 2012; Ng et al., 2013; Li et al., 2018; Shi et al., 2020; Meng et al., 2021). Sharma et al. (2001) performed a 2D finite element analysis of the effect of adjacent excavation on tunnel deformations. Also, Chen et al. (2016) investigated the stress and deformation pattern of a tunnel during excavation using 3D numerical simulation. Ng et al. (2013) examined the impact of excavation in a dry sand layer on underlying and lateral tunnels, and Zheng et al. (2010) investigated how excavation in dry sand strata affects the internal force and surrounding earth pressure on an underlying tunnel; both of these studies simulated basement excavation by draining heavy fluids away. Huang et al. (2014) investigated the effect of excavation on an underlying tunnel with 3D centrifuge model tests. Although Shanghai soft clay was used, their tests only considered the responses of the tunnel over a short period of excavation. The advantages of model testing over numerical simulation and field testing are mainly the lower cost, the ease of controlling and varying parameters, and the ease of comparative testing. Although experimental techniques such as centrifuge model testing and simulated excavation have seen success, existing centrifuge tests still have limitations, such as for cases of excavating foundation pits in normally consolidated soft clay layers, and for cases of in-flight excavation.

In this study, a centrifuge model test was performed for the excavation of a foundation pit, with an adjacent existing tunnel in a normally consolidated clay. Strong gravity of 120g was simulated during the test, where g is the gravitational acceleration. Following the backfilling of the tunnel with slurry, consolidation in the centrifuge was employed to create a uniformly and normally consolidated soft clay stratum. The undrained shear strength of the stratum, surface settlement behind the wall, longitudinal settlement of the tunnel, bending moment of the tunnel section, soil shear stiffness, pore water pressure, and lateral earth pressure were monitored and analyzed. Following the centrifuge test, a numerical model was developed for comparison with the testing results. Finally, a parametric study was conducted for the effect of the tunnel location on the variations of lateral earth pressure and pore water pressure above and at the side of the tunnel.

2 Testing setup

2.1 Centrifuge testing principle

The geotechnical centrifuge at Zhejiang University (ZJU-400) was used to conduct the centrifuge model test. The centrifuge has an effective rotation radius of 4.5 m, and an effective basket volume of 1.5 m×1.2 m×1.5 m. Its maximum capacity is 400 g·t, and the maximum centrifugal acceleration reaches 150g.

Centrifuge simulation enables the reduction of the model to 1/N of the prototype size; the equivalent centrifugal force field and gravity field concurrently amplify the volumetric force acting on the model by a factor of N. The corresponding scaling laws and centrifuge applications have been given by Schofield (1980) and Taylor (2018), and are detailed in Table 1. Under these conditions, the stress and strain at each point in the model align with those in the corresponding prototype.

Table 1 Centrifuge scaling laws

Item	Physical quantity	Scaling factor (model to prototype)
Gravity	Acceleration	N
Geometric characteristics	Geometric dimension	$1/N$
	Area	$1/N^2$
	Moment of inertia	$1/N^4$
Material properties	Elasticity modulus	1
	Density	1
	Quality	$1/N^3$
	Cohesive force	1
	Internal friction angle	1
	Bending stiffness	$1/N^4$
	Compression stiffness	$1/N^2$
Consolidation	Time	$1/N^2$

2.2 Testing materials

Fig. 1 presents the global view of the centrifuge model, with 1200 mm length, 1000 mm width, and 950 mm height. A 3D centrifuge model test was conducted, with a designed acceleration of 120g. In this model, commercial Malaysian kaolin clay was used as the testing material for the foundation soil, which has similar mechanical properties to the clays used by Purwana (2006), Xie et al. (2012), Taylor (2018), Alamanis et al. (2021), and Meng et al. (2021). Table 2 lists the basic properties for the kaolin clay, including

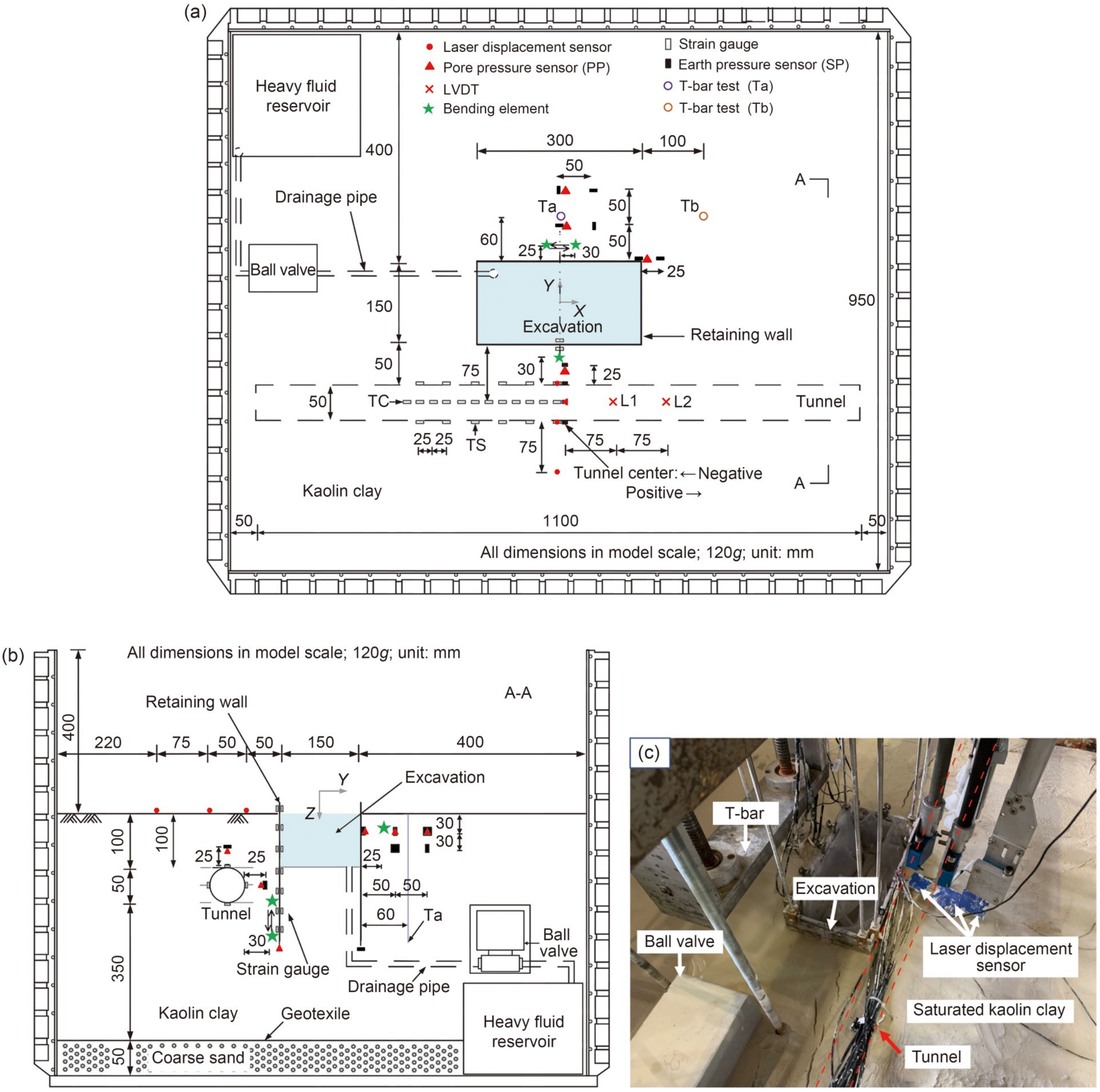

Fig. 1 Global view of the centrifuge model: (a) plan view (TC and TS indicate the strain gauges positions at the crown/bottom and side of the tunnel, respectively; LVDT indicates the linear variable differential transformer); (b) profile view; (c) photo from top of the model

its specific gravity, Atterberg's limit, coefficient of consolidation, permeability, and mechanical properties, as measured by consolidated-drained triaxial compression tests.

The tunnel model was built from an aluminium alloy tube, with an outer diameter *D* of 50 mm (6 m in prototype), a length of 1100 mm (132 m in prototype), a thickness of 1 mm (0.12 m in prototype), and a Young's modulus of 70 GPa (Fig. 1). Under the designed acceleration, the model tunnel had longitudinal and transverse stiffnesses equivalent to 143 mm and 151 mm thick slabs of concrete with Young's moduli of 35 GPa, respectively (Meng et al., 2021). The tunnel size aligns with the typical size of tunnels in China. The design buried depth was 100 mm (12 m in prototype), resulting in a cover-to-diameter ratio of 2.0, which is a common value in engineering practice (Ng et al., 2013; Chen et al., 2016; Meng et al., 2021).

The retaining wall was made of the same aluminum alloy material as the tunnel, with 300 mm length

(36 m in prototype) and 150 mm width (18 m in prototype) in plan view (Fig. 1a). The 5 mm thick aluminum with a Young's modulus of 70 GPa was equivalent to an 800 mm concrete slab in prototype (assuming a Young's modulus of 30 GPa in prototype), which aligned with those in Ng et al. (2013). The buried depth of the retaining wall was 240 mm (28.8 m in prototype). The specific model and prototype dimensions are shown in Table 3.

Table 2 Basic soil properties

Property	Value
Specific gravity	2.64
Liquid limit (%)	80
Plastic limit (%)	35
Coefficient of consolidation at 100 kPa (m^2/a)	40
Coefficient of permeability at 100 kPa (m/s)	2.0×10^{-8}
Effective cohesion (kPa)	3.8
Effective internal friction angle (°)	25.7
Unit weight (kN/m^3)	15.5–16.4

Note: Data from Lim (2004); Purwana (2006); Xie et al. (2012); Meng et al. (2021)

Table 3 Size for testing model and corresponding prototype

Model	Parameter	Model size (mm)	Prototype size (m)
Retaining wall	Length×width	300×150	36×18
	Thickness	5	0.6
	Excavation depth	100	12
	Insertion depth	160	19.2
Tunnel	Clear distance from excavation	50	6
	Outer diameter	50	6
	Length	1100	132
	Thickness	1	0.12
	Buried depth	100	12

2.3 Instrumentation

2.3.1 Measurement in clay

The distribution of the undrained shear strength S_u with depth was determined through a T-bar penetration test. The probe was 20 mm in length, with a diameter of 5 mm, a measuring range of 100 kPa, a maximum axial force of 440 N, and a maximum penetration depth of 0.5 m. The undrained shear strength was measured under static conditions. Two positions were selected for the test (Fig. 1): point Tb for the test before excavation, and point Ta for the test after excavation. Due to the dense arrangement of sensors, Ta was ultimately placed 60 mm (7.2 m in prototype) from the middle of the excavation. In addition, Tb was located at 250 mm on the Ta side, far from the excavation range.

Three laser displacement sensors were set behind the retaining wall (Fig. 1) to measure the surface settlement of the clay. The distances of these sensors to the nearby side of the retaining wall were 1D, 2D, and 3.5D, respectively (D is the outer diameter of the tunnel). To reflect the laser signal, small plastic sheets were placed at the corresponding positions on the ground.

Four earth pressure sensors were attached to the outer surface of the tunnel model at its midpoint (Fig. 1). Additionally, two sets of earth pressure-pore water pressure sensors were arranged near the tunnel model: one located at 25 mm (0.5D) above the crown in the middle of the tunnel, and another at 25 mm (0.5D) at the side of the tunnel. On the opposite side of the wall, nine earth pressure sensors were placed to track the variations in the earth pressure at various vertical and transverse locations around the foundation pit. Three pore water pressure sensors were deployed horizontally outside the retaining wall model, at a depth of 30 mm from the surface. Prior to sample preparation, all pore water pressure sensors were saturated.

Two pairs of bending elements were integrated into the corresponding polypropylene plates, attached to the side of the retaining wall (Fig. 1). One pair of the bending elements was used to measure the shear stiffness of the clay in the horizontal direction, and the other for the vertical direction. Sinusoidal signals with frequencies f=1.5 kHz and f=3 kHz were chosen as input signals through trial-and-error to ensure an optimal signal. The characteristic point method was applied to determine the transmission time of the shear wave, using the time difference between the first peak and the trough.

2.3.2 Measurement on the tunnel

Two linear variable differential transformers (LVDTs) were adopted to monitor the longitudinal settlement of the tunnel during the test. These LVDTs were positioned at intervals of 75 mm (1.5D) along the middle profile of the tunnel. Each LVDT was linked to an extension rod placed on the tunnel crown. To minimize friction, the surfaces of the extension rods were coated with silicone grease.

Strain gauges were positioned around the tunnel to monitor the longitudinal bending moments of the tunnel during the test (Fig. 1). The intervals between each group of TC and TS strain gauges were 25 mm (0.5*D*) and 50 mm (1*D*), respectively. In total, 18 groups of strain gauges (including both TC and TS) were attached to the outer surface of the tunnel. To enhance sensitivity and ensure accurate measurements, all the strain gauges were configured into a Wheatstone half-bridge circuit. Before the test, the calibration coefficients between the bending moment (theoretical calculation) and the strain data (from the acquisition system) were established by performing loading at the center of the tunnel.

2.3.3 Measurement on the retaining wall

Seven pairs of strain gauges were attached vertically to the inner and outer surfaces along the centerline of the retaining wall (Fig. 1). The configuration of each pair of the strain gauges was similar to the sensor positions on the tunnel. During the test, the bending moments along the retaining wall were measured, allowing the lateral displacement of the retaining wall to be calculated.

3 Testing methods

3.1 Sample preparation

First, for effective water drainage during consolidation, a 50 mm thick sand layer was positioned beneath the clay layer. Drainage pipes were placed at the base, with the surplus extending outward along the corners of the model box. Second, the sand was covered by geotextile, and the reservoir was placed at the bottom. Third, the slurry was prepared by mixing kaolin with water to reach twice the liquid limit. After 72 h of moisture homogenization, the kaolin slurry was poured into the model box. And after a 48 h standing period, the excess water was drained from the top, followed by stratified static consolidation in the centrifuge. The evolution of pore water pressure during consolidation is depicted in Fig. 2. It can be observed that the change in pore water pressure in the final stage of consolidation accounts for less than 10% of the total variation, suggesting that the degree of soil consolidation exceeded 90% and the consolidation of the stratum was largely completed (Lam, 2010; Meng et al., 2021). In order to avoid disturbance to the shallow stratum during the installation of the retaining wall and tunnel, the stratum was excavated to the depth of the crown. Then, the soil in the tunnel was excavated to install the tunnel model, and the retaining wall model was squeezed into the design depth. At the same time, the ball valve and pipes were connected. Later, the saturated slurry was re-injected and consolidated to the designed height in the centrifuge. Similar monitoring of the pore water pressure as in Fig. 2 was performed to ensure the consolidation was largely completed (defined as the degree of consolidation exceeding 90%). Finally, the residual sensors were installed, flexible rubber was used to replace the inside stratum of the retaining wall model, and it was filled with heavy liquid (Shi, 2015).

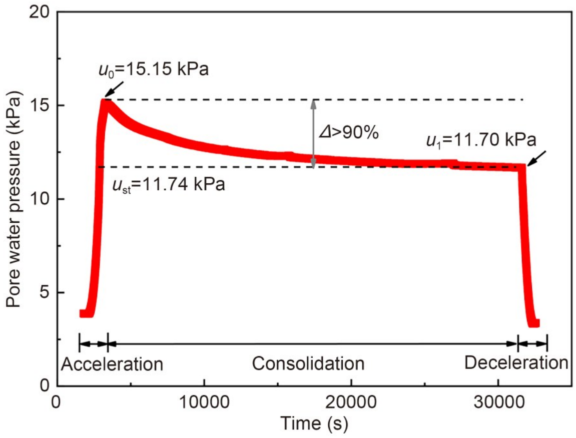

Fig. 2 Evolution of pore water pressure with time for consolidation of soil. u_0 is the initial pore water pressure; u_1 is the final pore water pressure; u_{st} is the stable pore water pressure; Δ is the change of pore water pressure

3.2 Testing procedures

Following the preparation of the centrifuge model, the model box was elevated onto the centrifuge platform. Initially, a T-bar test was conducted at the Tb position under 1*g* gravity. Subsequently, the centrifuge acceleration was gradually increased to 120*g*. After the centrifuge acceleration stabilized at 120*g*, the centrifuge was maintained for around 10 min (60 d in prototype) to eliminate the negative impacts of sensor installation and centrifuge acceleration on data stability. The heavy liquid ($ZnCl_2$ solution) method was selected to replicate the excavation (Shi, 2015). The drainage lasted for 5 min, corresponding to 30 d for the prototype, which is equivalent to 0.4 m/d as observed in a foundation pit in Shanghai in 2012 (Ng et al., 2012). After the excavation was completed, the centrifuge operated continuously for 2.5 h, replicating the conditions 4 a after excavation in a practical project. Throughout the testing process, the wave velocity of bending elements was measured manually, before and after the excavation. The testing data were automatically recorded and saved by the centrifuge's digital signal acquisition system. Finally, the acceleration of the centrifuge was gradually decreased to 1*g*. Immediately upon reaching normal gravity, a T-bar test was conducted at the Ta position.

4 Interpretation of the testing results

The subsequent model testing results are converted into equivalent prototype values to present the outcomes in a straightforward manner. The results primarily encompass the undrained shear strength of the stratum, surface settlement behind the wall, longitudinal settlement of the tunnel, bending moment of the tunnel section, stratum shear stiffness, pore water pressure, and lateral earth pressure.

4.1 Analysis of bending moment

In this section, the effects of excavation and the long-term period following excavation on the bending moment of the tunnel and the retaining wall are analyzed.

4.1.1 Longitudinal bending moment of the tunnel

Fig. 3 displays the vertical and horizontal bending moments of the tunnel along the longitudinal direction. During the test, only some of the strain gauges were operating correctly, which are shown as filled signs on the tunnel in Fig. 3. It can be seen that the excavation leads to the development of the longitudinal bending moment of the tunnel, through the deformation of the retaining wall towards the pit. Regarding the measurement by the sensors of TC in Fig. 1, the vertical bending moment is relatively uniform along the longitudinal distribution, both within and outside the excavation range (Fig. 3a). In addition, with the increase of the elapsed period (t_p) after excavation, the vertical bending moment increases at a given location. The value of the bending moment at the center reached 9.20 kN·m at 1200 d, which was approximately twice the value at t_p=0 d (5.57 kN·m). Overall, the vertical bending moment is smaller than 20 kN·m.

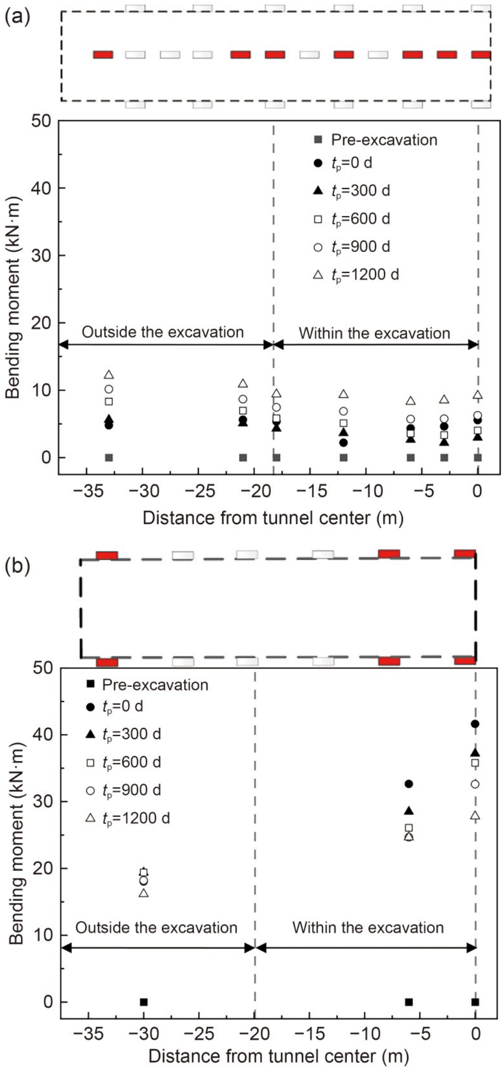

Fig. 3 Distribution of the bending moment of the tunnel in the longitudinal direction: (a) vertical bending moment (TC); (b) horizontal bending moment (TS)

In contrast, the value of the horizontal bending moment is higher than the vertical bending moment at the corresponding location of the tunnel, particularly within the excavation range (Fig. 3b). Furthermore, the distribution of the horizontal bending moment is not uniform along the longitudinal direction of the tunnel, showing a significant value within the excavation range (41.64 kN·m at the center, and 18.04 kN·m at 30 m). This suggests that after excavation, the bending moment develops around the tunnel at the side of the excavation. Moreover, special attention should be paid to the higher horizontal bending moment within the excavation range. Notably, for almost all positions measuring the horizontal bending moment, the value decreased during the elapsed period, with reductions of approximately 13.82 kN·m at the center and 1.87 kN·m at 30 m. This decline was likely due to clay displacement.

4.1.2 Bending moment and horizontal deformation of the retaining wall

Fig. 4 depicts the distribution of the bending moment and the horizontal deformation at the center of the retaining wall along the depth. In this figure, negative values for the bending moment and horizontal deformation indicate those oriented towards the pit. After excavation, the retaining wall exhibits an inward bending moment and horizontal deformation, showing a cantilever deformation pattern. The bending moment in the center of the retaining wall was 7.30 kN·m after excavation, and the maximum bending moment occurred at the bottom with −75.93 kN·m. Subsequently, the central bending moment decreased to 3.86 kN·m, and the bottom bending element increased significantly to −10.93 kN·m. Below the excavation range, negligible horizontal deformation can be identified, thus resulting in higher values of the bending moment. In contrast, above the excavation range, the horizontal deformation increases, with a higher value moving away from the bottom of the excavation. The displacement of the retaining wall near the ground surface into the pit reached 0.22 m after excavation, and then increased to 0.37 m at the end of the test. After excavation, the increasing rate of the horizontal deformation of the retaining wall is about 3.6 mm/month, which is slightly higher than the value of 3.0 mm/month found by Finno et al. (2019) in the case of Chicago medium stiff clay. In addition, the elapsed period after excavation has a limited influence on the variations of the bending moment of the retaining wall/tunnel and the horizontal deformation of the retaining wall.

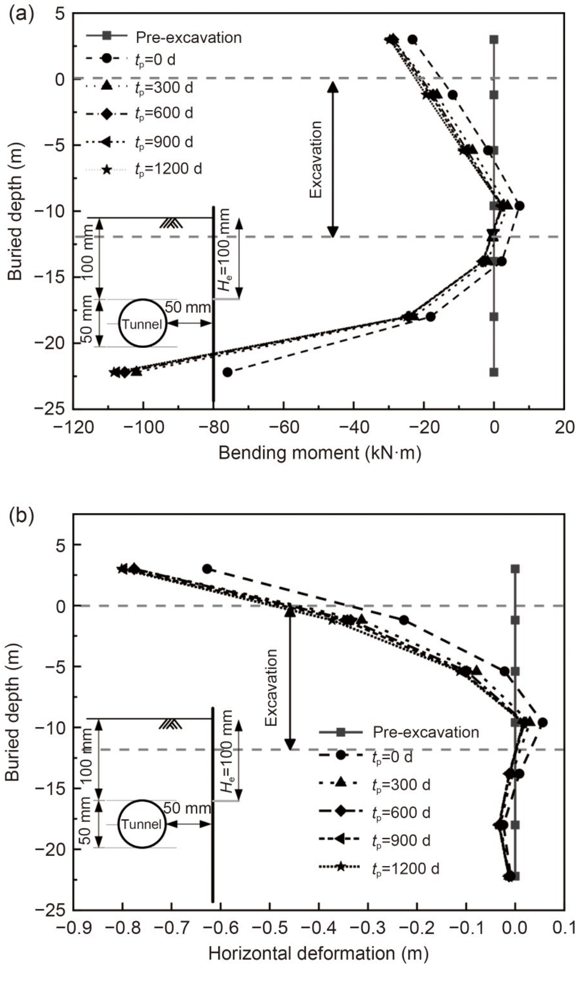

Fig. 4 Distributions of (a) bending moment and (b) horizontal deformation of the retaining wall along the depth

4.2 Analysis of settlement

4.2.1 Ground surface settlement

The evolution of the ground surface settlement behind the retaining wall with respect to the elapsed period is shown in Fig. 5. It can be observed that after excavation, the ground surface settlement increases rapidly at each sensor behind the retaining wall. As the elapsed period following excavation increases, the ground surface settlement continues to increase, at the rates of 0.24 mm/d, 0.18 mm/d, and 0.22 mm/d for sensors J1, J2, and J3, respectively. Comparing with the settlement rate in Meng et al. (2021), these increasing rates indicate that the normally consolidated clay was softer than the over-consolidated clay stratum. In addition, no stiff structure was installed at the bottom of the foundation pit after excavation, due to the limitations of the centrifuge test. This might lead to a sliding flow of the surrounding soil into the foundation pit, causing extra settlement. In addition, the distribution of the ground surface settlement behind the retaining wall shows a convex pattern, with the settlement for J2 being the lowest. This may be induced by the existence of the tunnel, which prohibits settlement development at sensor J2 above the tunnel. In addition, due to the deformation mode of the retaining wall and the positions of the sensors, the settlement amount and rate at J1 are greater than at J3.

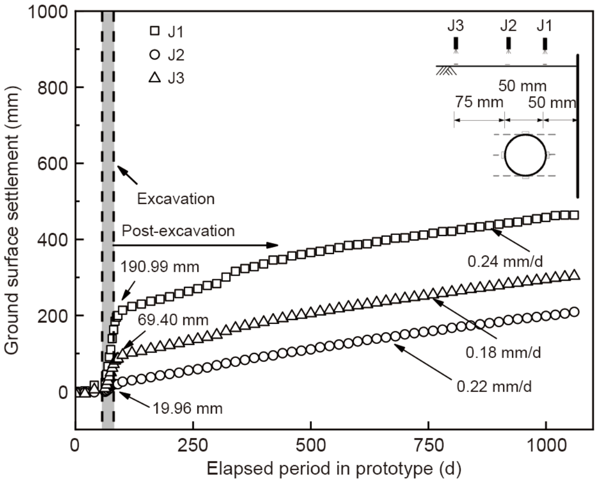

Fig. 5 Evolution of the ground surface settlement behind the retaining wall with the elapsed period

4.2.2 Tunnel settlement

Fig. 6 depicts the variations of the settlement on the tunnel (L1 and L2; see detailed locations in Fig. 1a) with differing elapsed periods. During excavation, negligible settlement can be identified at both measuring points on the tunnel. As the elapsed period after excavation increases, the settlement increases at a stable rate at each sensor, which is attributed to the sliding flow of the surrounding stratum into the excavation range. Owing to the sustained rise in ground subsidence observed in Fig. 5, the tunnel experienced comprehensive settlement. Concurrently, the longitudinal differential settlement within the tunnel was mitigated. Also, compared to the ground settlement in Fig. 5, the settlement on the tunnel here was smaller.

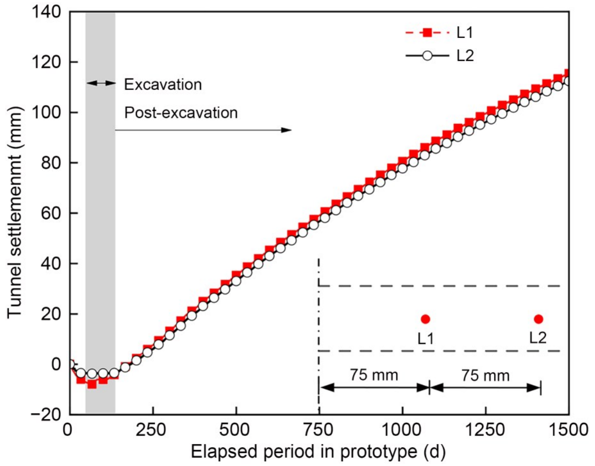

Fig. 6 Evolution of the settlement on the tunnel with the elapsed period

4.3 Soil testing and analysis

4.3.1 Undrained shear strength of the soil

Fig. 7 shows the results of the T-bar testing. The results for Tb correspond to the normally consolidated clay after the centrifuge consolidation but before excavation, while those for Ta are for the case after the test. It can be seen that the undrained shear strength at Tb exhibits a linear increase with depth. Furthermore, the curve for Tb is continuous, demonstrating that the secondary slurry is well consolidated. A fitting line can be plotted for Tb to reflect the preparation condition of clay, which gives the relationship between the undrained shear strength S_u and the effective earth pressure σ_v' as:

$$S_u = 0.19\sigma_v'. \tag{1}$$

The fitting slope of 0.19 is slightly smaller than that for clay in Taipei, China ($S_u = 0.22\sigma_v'$) (Lim et al., 2010), and slightly larger than that for clay in Ningbo, China ($S_u = 0.14\sigma_v'$) (Li, 2015). Instead of undrained shear strength as shown by Meng et al. (2021), the curve for Ta within the excavation depth is close to that of Tb. This may be due to the over-consolidation of the surface layer within 8 m, resulting in a more pronounced difference between Ta and Tb than in our results.

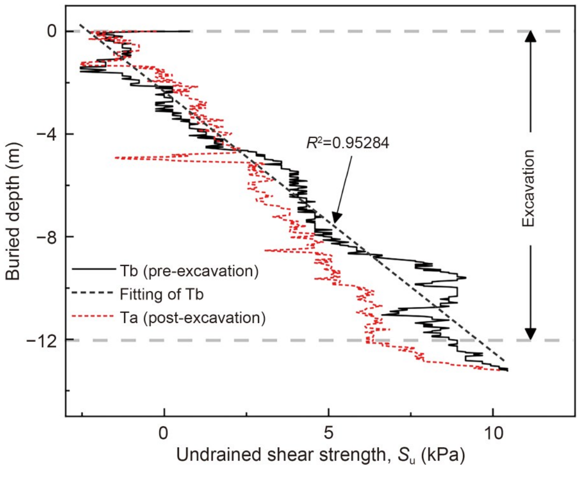

Fig. 7 Distribution of undrained shear strength of soil along the depth

4.3.2 Shear stiffness between the tunnel and retaining wall

Using the characteristic point method, the propagation time *t* of the shear wave transmitted in the soil can be obtained from the signal measured by the bending elements. Thus, the shear wave velocity V_s can be calculated as:

$$V_s=L/t, \tag{2}$$

where L is the distance between bending elements (60 mm, as shown in Fig. 1). Then, the small-strain shear stiffness G_0 can be determined as:

$$G_0=\rho V_s^2, \tag{3}$$

where ρ is the density of the soil.

For validation, the initial shear stiffness proposed by Rampello et al. (1997) is also calculated as:

$$\frac{G_0}{P_a}=Sf(e)\left(\frac{p'}{P_a}\right)^n, \tag{4}$$

where $f(e)$ is the void ratio function, equal to $f(e)=(1+e)^{-2.4}$ for clay (Shibuya et al., 1997); e is the void ratio; p' is the average effective stress of the soil; P_a is the reference stress; S is a stiffness multiplier for the isotropic stress history; n is the exponent of mean effective stress.

Fig. 8 plots the variations of the soil shear stiffness at different sensors beside the retaining wall (BES1–BES4 represent the bending element sensors). The measured data of the initial shear stiffness correspond to the data in Rampello et al. (1997), validating the accuracy of the centrifuge model test. During excavation, the increment of the shear stiffness is similar for the two pairs of bending elements. After excavation, the shear stiffness in the vertical direction of the deeper soil increases with the elapsed period, while that in the horizontal direction of the shallower soil stays relatively stable with increasing time. This is because during the period after excavation, the soil outside the retaining wall tends to move towards the wall in a circumfluent manner, densifying the soil in the vertical direction between the bending elements in Fig. 8a. However, the soil is not densified in the horizontal direction for the sensors in Fig. 8b, resulting in stable shear stiffness values with respect to the elapsed period. Furthermore, for deeper soil (which likely has a higher degree of consolidation), the shear stiffness is higher than at shallower depths.

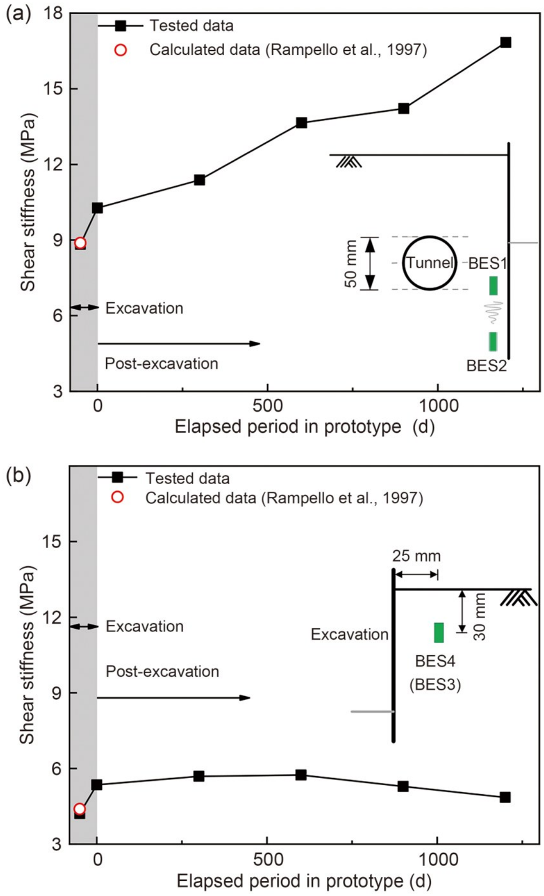

Fig. 8 Evolution of the shear stiffness in the soil for different sensors beside the retaining walls with the elapsed period: (a) shear stiffness in the vertical direction; (b) shear stiffness in the horizontal direction

4.3.3 Analysis of pressure around the tunnel

The variations of the relative lateral earth pressure at the side of the tunnel with respect to the elapsed period are shown in Fig. 9. In this study, the relative lateral earth pressure is defined as the difference between the lateral earth pressure at a given elapsed period and its initial value. During excavation, the lateral earth pressure at the sensor close to the excavation (SP2) decreases significantly, while the decrease at the sensor away from the excavation (SP4) is less pronounced. After excavation, the value at SP2 first increases and then decreases. The value at SP4 continues to decrease. After 400 d, the two values approach a similar trend.

Fig. 10 illustrates the development of the excess pore water pressure (P_p) and relative lateral earth pressure (P_s) in the soil around the tunnel. In this figure, the sensor captions of PP and SP represent the pore water pressure sensor and soil pressure sensor,

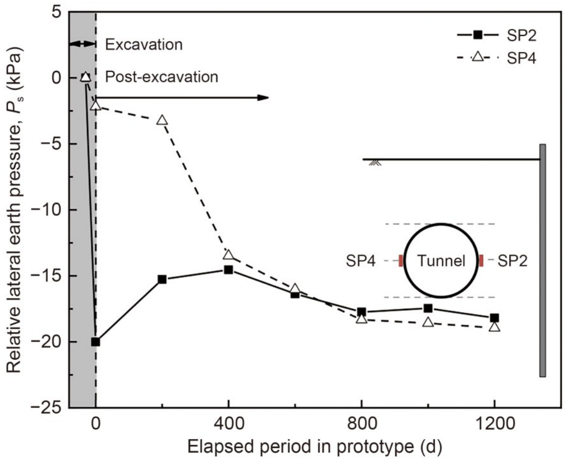

Fig. 9 Evolution of the relative lateral earth pressure at the side of the tunnel with the elapsed period

respectively. It can be observed in Fig. 10a that the excavation leads to the development of negative excess pore water pressure and the decrease of the lateral earth pressure. During the elapsed period after excavation, the lateral earth pressure gradually increases at both locations, while the excess pore water pressure remains relatively stable (Fig. 10). In other words, the excavation process induces the unloading effect, which is followed by the recovery of the effective lateral earth pressure (an increasing amplitude of 6.9 kPa above the crown and 13.7 kPa on the side) over a long-term period after excavation. This variation trend is probably caused by the squeezing effect of the soil between the tunnel and the retaining wall.

4.3.4 Analysis of pressure behind the wall

The evolution of the relative lateral earth pressure and the excess pore water pressure behind the retaining wall at 3.6 m depth is presented in Fig. 11. As shown, due to the excavation, the negative excess

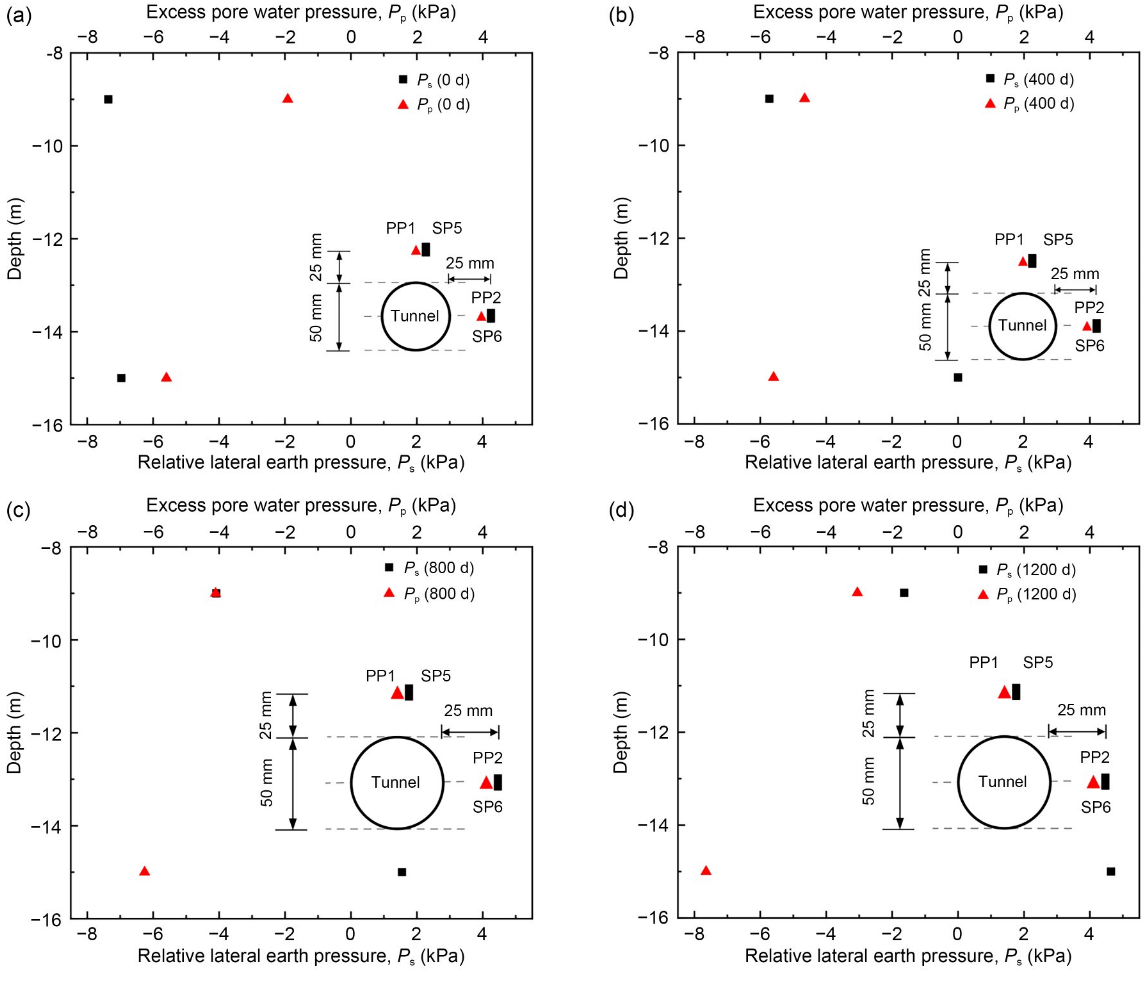

Fig. 10 Distributions of the relative lateral earth pressure and the excess pore water pressure around the tunnel for different elapsed periods: (a) t_p=0 d; (b) t_p=400 d; (c) t_p=800 d; (d) t_p=1200 d

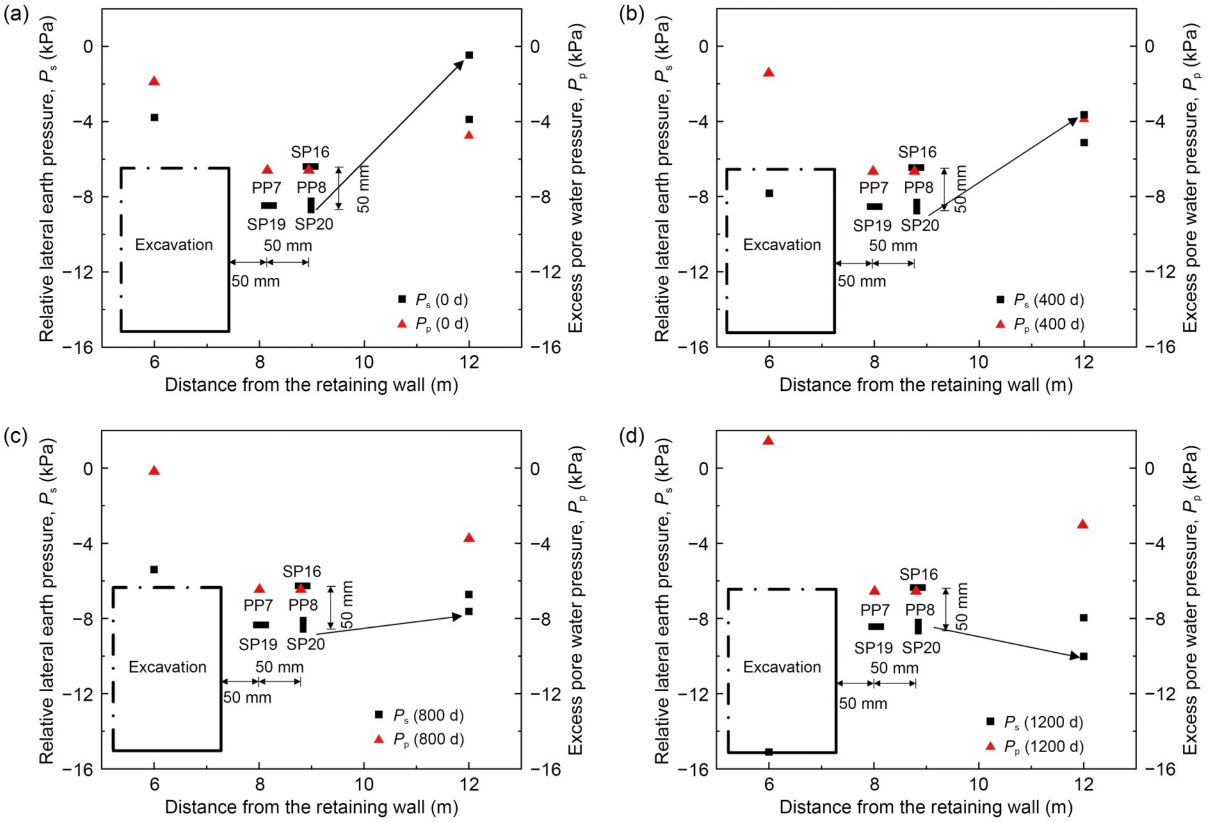

Fig. 11 Evolution of the relative lateral earth pressure and the excess pore water pressure behind the retaining wall at 3.6 m depth: (a) t_p=0 d; (b) t_p=400 d; (c) t_p=800 d; (d) t_p=1200 d

pore water pressure and the decrease of the lateral earth pressure still occur. However, during the period after excavation, the pore water pressure increases slightly, but the lateral earth pressure continues to decrease, which is different from the sensors around the tunnel shown in Fig. 10. This is because in the elapsed period, the soil continues to move towards the excavation area, as evidenced by the settlement development in Figs. 5 and 6. No squeezing effect of the soil can be supported behind the retaining wall, which leads to the variation trend of the lateral earth pressure and pore water pressure presented in Fig. 11. The evolution of the relative lateral earth pressure behind the retaining wall at 7.2 m depth is shown in Fig. 12, with a similar variation trend as behind the retaining wall in Fig. 11.

5 Numerical simulation

5.1 Overview of the numerical model

To better understand the effect of excavation on the nearby underground structure, a numerical model was developed using the software PLAXIS 3D (Plaxis, 2002). The model development matched the testing conditions in our centrifuge model test. In the numerical simulation, the parameters were derived from the prototype parameters corresponding to the model test. The size of the model was set as 144 m×114 m×72 m (length×width×height), as shown in Fig. 13. The distance between the boundaries of the numerical model and the tunnel/retaining wall was kept large enough to diminish boundary effects. Specifically, the bottom boundary of the model was located 5 times the excavation depth below the foundation pit, while the side boundary was approximately 5 times the tunnel diameter (D) away from the tunnel. The top of the model was set as a free boundary, while the sides and the bottom of the model were set with hinge and fixed constraints, respectively. Simultaneously, seepage boundaries were opened on the top and the bottom of the model, while the boundaries for the sides of the model were closed. The groundwater level was situated at the top of the model, indicating the soil was saturated. The finite element model was then validated

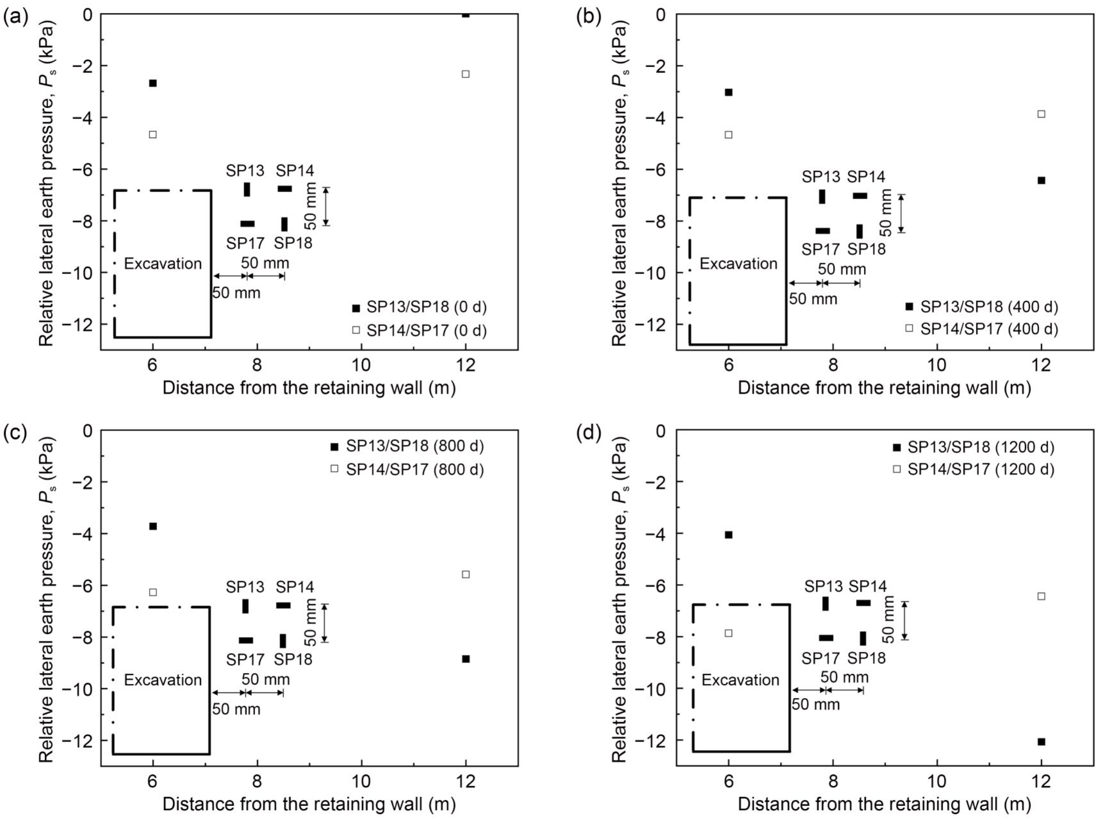

Fig. 12 Evolution of the relative lateral earth pressure behind the retaining wall: (a) t_p=0 d; (b) t_p=400 d; (c) t_p=800 d; (d) t_p=1200 d

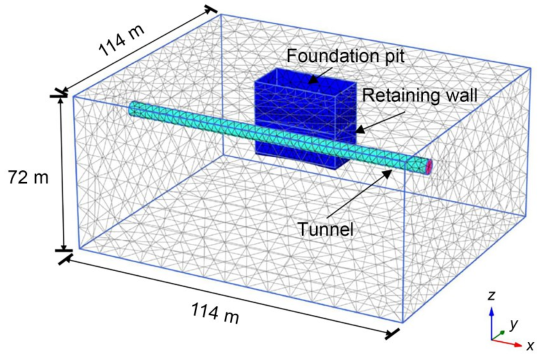

Fig. 13 Model overview for the numerical simulation

against the centrifuge test (Liu, 2020; Meng et al., 2021). The numerical model was adjusted according to the centrifuge test, with the clay and model parameters remaining consistent as obtained through the 1D standard consolidation test and the consolidated undrained triaxial test (Meng et al., 2021). The remaining basic soil parameters, such as unit weight, coefficient of consolidation, and coefficient of permeability, came from literature on Malaysian kaolin recorded by Lim (2004), Purwana (2006), and Xie et al. (2012).

5.2 Material properties

In this centrifuge model test, Malaysian kaolin was employed to replicate a clay stratum (Anagnostopoulos et al., 2020). In the numerical simulation, a hardening soil model with small-strain stiffness (HSS model) was used, which has been extensively applied in numerical simulations of clay (Wang et al., 2013; Alamanis et al., 2021). Table 4 lists the model parameters for the kaolin.

The PLAXIS 3D Tunnel Designer was employed for tunnel generation, with the tunnel lining constituted by 6-node plate elements. The outer diameter and the length of the tunnel were 6 m and 112 m, respectively. The behaviour of the surface flow boundary condition of the tunnel was set to be closed, with the corresponding model parameters listed in Table 5. The retaining wall was similarly modelled using the 6-node plate elements. Aligning with the prototype parameters derived from the centrifuge test, the foundation pit had a depth of 31 m, a length of 36 m, a width of 18 m, and an equivalent thickness of 0.8 m. Table 5 also lists the model parameters for the retaining wall.

Table 4 HSS model parameters for the kaolin

Parameter	Value	Parameter	Value
$E_{\mathrm{oed}}^{\mathrm{ref}}$ (MPa)	1.9	R_{f}	0.9
E_{50}^{ref} (MPa)	1.9	m	0.83
$E_{\mathrm{ur}}^{\mathrm{ref}}$ (MPa)	8.36	K_0	0.61
c' (kPa)	2	υ_{ur}	0.2
φ' (°)	23	G_0 (MPa)	29.5
ψ (°)	0	$\gamma_{0.7}$	2×10^{-4}

Note: $E_{\mathrm{oed}}^{\mathrm{ref}}$ is the tangent stiffness for the primary oedometer loading; E_{50}^{ref} is the secant stiffness from a standard drained triaxial test; $E_{\mathrm{ur}}^{\mathrm{ref}}$ is the unloading/reloading stiffness from a drained triaxial test; c' is the effective cohesion; φ' is the effective friction angle; ψ is the dilatancy angle; R_{f} is the failure ratio (default is 0.9); m is the power exponent of the stiffness stress level correlation; K_0 is the coefficient of the static lateral pressure under normal consolidation conditions; υ_{ur} is the unloading/reloading Poisson's ratio (default is 0.2); G_0 is the reference shear modulus at very small strains ($\varepsilon<10^{-6}$); $\gamma_{0.7}$ is the shear strain corresponding to the attenuation of the secant shear modulus to 70% of the initial shear modulus

5.3 Simulation procedures

Initially, the in-situ stress field was established for the numerical simulation before excavation. Then, a tunnel was generated to simulate tunnel excavation. Subsequently, a 100-d consolidation period was initiated to stabilize the earth pressure and pore water pressure surrounding the tunnel. Upon completion, the retaining wall was installed. The displacements were reset to zero, with another 100-d consolidation calculation performed to represent stabilization (similar to the actual stabilization time), which minimizes the disturbance from the tunnel generation. After that, the soil inside the retaining wall was replaced with a surface load to simulate the heavy liquid. The surface load was removed to simulate the excavation process, corresponding to a 30-d prototype duration. Finally, upon completion of the excavation, the simulation was terminated when the elapsed period reached 1200 d. The calculation of the pore water pressure from the previous step was used for the deformation calculation in the subsequent step. During the numerical simulation, the lateral earth pressure and pore water pressure in the model were measured.

5.4 Numerical comparison

Fig. 14 presents a comparison between the testing results from the present centrifuge tests and the calculated results from the numerical simulation, regarding the variation of the relative lateral earth pressure with the elapsed period. Overall, the calculated results show strong agreement with the measurements. Due to the movement of soil to the excavation range, the relative lateral earth pressure decreases with the elapsed period for both the measured and calculated values.

Next, the variation of the excess pore water pressure with the elapsed period for both the testing results and numerical results is shown in Fig. 15. Similarly, consistency is found between the measured and calculated results, illustrating the robustness and accuracy of our numerical modelling.

5.5 Parametric study

To achieve a better understanding of the effect of the tunnel location on the variations of relative lateral earth pressure and excess pore water pressure, parametric studies are conducted. The basic soil parameters are given in Table 4, and the basic parameters for the tunnel and the retaining wall are shown in Table 5, with the plate element adopted for these two structures. Fig. 16 shows the four cases for the parametric study, including three tunnel locations (Cases 1, 2, and 3) and Case 4, where a bottom plate is added based on Case 1. Two measuring points are set around the tunnel: point *A* above the crown of tunnel 1, and point *B* at the side of tunnel 1. Note that Case 1 corresponds to the present centrifuge model test.

5.5.1 Relative lateral earth pressure

Fig. 17 shows the evolution of the relative lateral earth pressure around the tunnel with the elapsed period. Upon excavation, the relative lateral earth pressure decreases rapidly. During the elapsed period, the relative lateral earth pressure only changes slightly for all the cases. In comparison with point *A*, the decreasing

Table 5 Model parameters for the tunnel and the retaining wall

Structure	Equivalent diameter (m)	Equivalent thickness (m)	Elastic modulus in the 1st and 2nd axial directions (kN/m^2)	Equivalent weight (kN/m^3)	Poisson's ratio
Tunnel	6	0.15	7.20×10^7	27.2	0.15
Retaining wall	NA	0.8	7.20×10^7	27.0	0.15

NA: not applicable

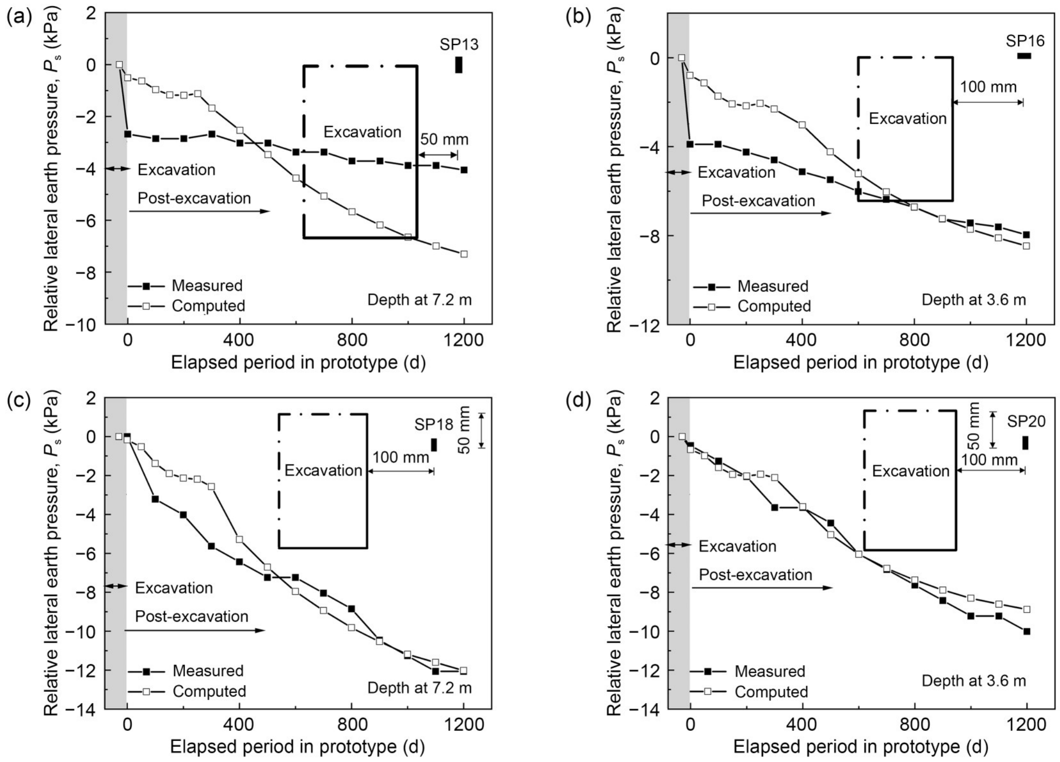

Fig. 14 Comparison of the relative lateral earth pressure between measured and computed results: (a) SP13; (b) SP16; (c) SP18; (d) SP20

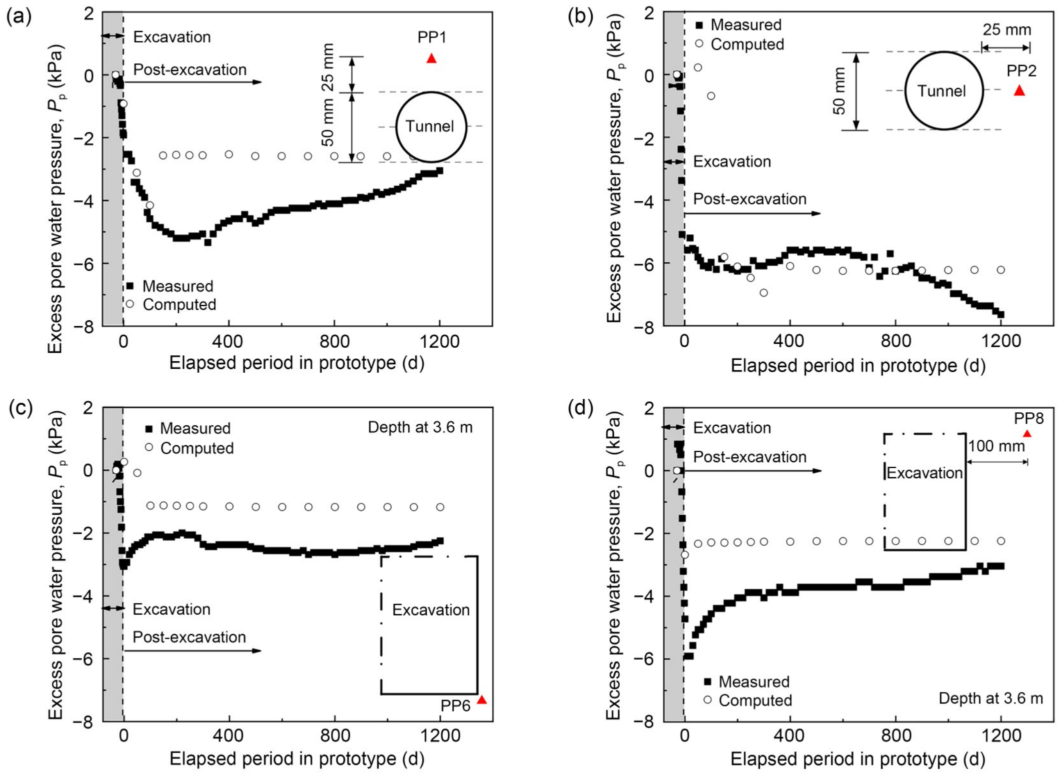

Fig. 15 Comparison of the excess pore water pressure between measured and computed results: (a) PP1; (b) PP2; (c) PP6; (d) PP8

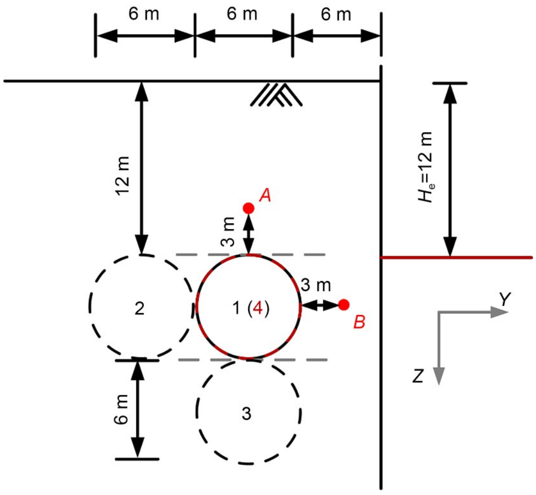

Fig. 16 Diagram of different calculation cases

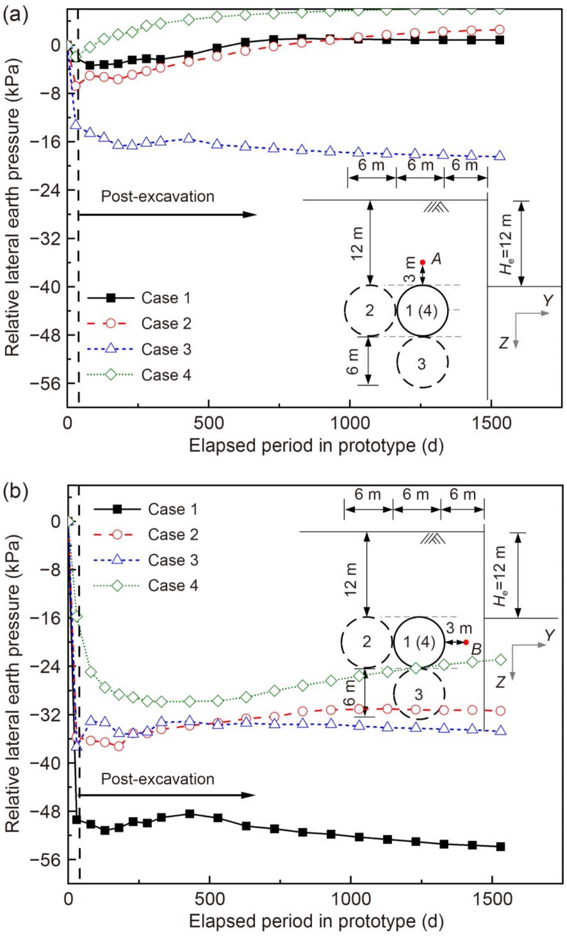

Fig. 17 Evolution of the relative lateral earth pressure with the elapsed period around the tunnel at (a) point *A* and (b) point *B*, for the four cases

amplitude of the relative lateral earth pressure at point *B* is more significant, because point *B* is closer to the excavation range. At point *A*, the decreasing amplitude of the relative lateral earth pressure has the greatest magnitude for Case 3 and the smallest magnitude for Case 4, while the variation of the relative lateral earth pressure shows a similar trend for Cases 1 and 2. This is probably because the soil arching effect occurs after the excavation of the retaining wall, and the horizontal deformation of the tunnel affects the range. Moreover, the difference in buried depth leads to a change in the soil arching effect and a significant change in lateral earth pressure at point *A*. In contrast, at point *B*, the decreasing amplitude of the relative lateral earth pressure is most significant for Case 1, whereas Cases 2 and 3 have a similar variation trend. The change for Case 4 (where the bottom plate is applied) is the smallest, which is consistent with the result at point *A*. The lateral earth pressure at point *B* is influenced not only by soil compression, but also by the deformation of the retaining wall. The closer the point is to the tunnel, the greater the variation in earth pressure during excavation. After excavation, all the relative lateral earth pressures change slightly with the elapsed period.

5.5.2 Excess pore water pressure

The evolution of the excess pore water pressure around the tunnel with respect to the elapsed period is presented in Fig. 18. For all cases, the excess pore water pressure decreases around the tunnel during excavation, followed by a gradual dissipation after excavation. During excavation for a given case, the change of the excess pore water pressure at point *B* is greater than that at point *A*. This phenomenon becomes less obvious as the measuring point moves farther away from the tunnel. For both measuring points, the decreasing amplitude of the excess pore water pressure is more significant for Case 1 during excavation. After excavation, horizontal deformation of the tunnel and the retaining wall immediately occurs. Thus, Case 1 (with the tunnel closest to the excavation) results in more significant variation of the excess pore water pressure. For the pore water pressure above the crown, the excess pore water pressure gradually dissipates to 0 during the elapsed time. In Case 4, due to the undrained boundary at the bottom, the excess pore water pressure does not dissipate completely, which is consistent with the results of all cases at point *B*.

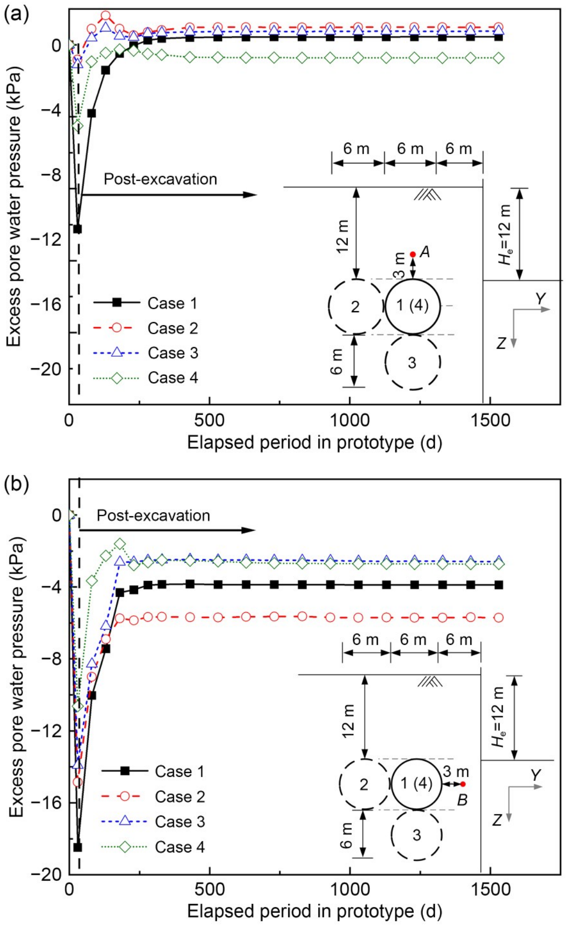

Fig. 18 Evolution of the excess pore water pressure with the elapsed period around the tunnel at (a) point *A* and (b) point *B*, for the four cases

6 Conclusions

A centrifuge model test and numerical simulations were conducted to investigate the effect of excavation on an existing adjacent tunnel in a normally consolidated clay stratum. The test replicated excavation under 120*g* gravity, providing insights into the short- and long-term responses of the existing tunnelling and surrounding stratum.

We found that the excavation significantly affects the horizontal deformation of the retaining wall and tunnel. However, over a long-term period after excavation, the horizontal deformation of the retaining wall and tunnel stabilizes, with only slight variations observed after excavation. Notably, the long-term elapsed period has a more significant impact on ground surface settlement and tunnel settlement. These changes are more pronounced compared to the horizontal deformation. During excavation, the negative excess pore water pressure increases, and the lateral earth pressure decreases around the excavation range. In the soil between the tunnel and retaining wall, the excess pore water pressure remains relatively stable, while the lateral earth pressure gradually increases during the long-term period after excavation due to the soil's squeezing effect. At other measuring locations, the pore water pressure increases slightly, while the lateral earth pressure continues to decrease after excavation.

Our numerical modelling showed that excavation leads to a reduction in both the lateral earth pressure and the pore water pressure. Through the elapsed period, the lateral earth pressure stays relatively stable, while the excess pore pressure dissipates gradually. When the tunnel is closer to the retaining wall, the decreases in lateral earth pressure and pore water pressure during excavation are more pronounced. However, the variations of the lateral earth pressure and pore water pressure above the tunnel are inconsistent, which may be related to the soil arching effect caused by the combined deformation of the tunnel and excavation.

These findings can be adopted for predicting and mitigating the impact of excavation on existing tunnels. They might also act as a technical reference for the design and construction of retaining walls and tunnels in similar geological conditions, enhancing safety and efficiency in urban excavation projects. However, a few limitations should be noted. First, due to the limitations of centrifuge testing, it is challenging to fully replicate the installation of a stiff structure at the bottom of a foundation pit after excavation. This may lead to extra settlement of the surrounding stratum. Second, the overly dense arrangement of sensors might disturb the testing results. Finally, the extensive testing period and complicated centrifuge setup permitted only one test. Additional tests and broader investigations should be performed to gain more insights.

Acknowledgments

This work is supported by the National Natural Science Foundation of China (Nos. 52378341, 51938005, and 52090082).

Author contributions

Ren-Peng CHEN, Yong XU, Han-Lin WANG, and Fan-Yan MENG designed the research. Yong XU and Han-Lin WANG processed the corresponding data. Yong XU wrote the first draft of the manuscript. Han-Lin WANG helped to organize the manuscript. Yong XU, Han-Lin WANG, and Fan-Yan MENG revised and edited the final version.

Conflict of interest

Ren-Peng CHEN, Yong XU, Han-Lin WANG, and Fan-Yan MENG declare that they have no conflict of interest.

References

Alamanis N, Lokkas P, Chrysanidis T, et al., 2021. Assessment principles for the mechanical behavior of clay soils. *WSEAS Transactions on Applied and Theoretical Mechanics*, 16:47-61. https://doi.org/10.37394/232011.2021.16.6

Anagnostopoulos CA, Chrysanidis T, Anagnostopoulou M, 2020. Experimental data of cement grouting in coarse soils with different superplasticisers. *Data in Brief*, 30:105612. https://doi.org/10.1016/j.dib.2020.105612

Chen RP, Meng FY, Li ZC, et al., 2016. Investigation of response of metro tunnels due to adjacent large excavation and protective measures in soft soils. *Tunnelling and Underground Space Technology*, 58:224-235. https://doi.org/10.1016/j.tust.2016.06.002

Chen RP, Liu QW, Wang HL, et al., 2021. Performance of geosynthetic-reinforced pile-supported embankment on soft marine deposit. *Proceedings of the Institution of Civil Engineers-Geotechnical Engineering*, 174(6):627-644. https://doi.org/10.1680/jgeen.19.00136

Cheng HZ, Chen RP, Wu HN, et al., 2020. A simplified method for estimating the longitudinal and circumferential behaviors of the shield-driven tunnel adjacent to a braced excavation. *Computers and Geotechnics*, 123:103595. https://doi.org/10.1016/j.compgeo.2020.103595

Finno RJ, Kim S, Lewis J, et al., 2019. Observed performance of a sheetpile-supported excavation in Chicago clays. *Journal of Geotechnical and Geoenvironmental Engineering*, 145(2):05018005. https://doi.org/10.1061/(asce)gt.1943-5606.0002010

Gao BY, Chen RP, Wu HN, et al., 2024. Investigation of mechanical failure performance of a large-diameter shield tunnel segmental ring. *Journal of Zhejiang University-SCIENCE A*, 25(5):411-428. https://doi.org/10.1631/jzus.A2300446

Hsieh PG, Ou CY, 1998. Shape of ground surface settlement profiles caused by excavation. *Canadian Geotechnical Journal*, 35(6):1004-1017. https://doi.org/10.1139/t98-056

Huang X, Huang HW, Zhang DM, 2014. Centrifuge modelling of deep excavation over existing tunnels. *Proceedings of the Institution of Civil Engineers-Geotechnical Engineering*, 167(1):3-18. https://doi.org/10.1680/geng.11.00045

Lam SY, 2010. Ground Movements Due to Excavation in Clay: Physical and Analytical Models. PhD Thesis, University of Cambridge, Cambridge, UK. https://doi.org/10.17863/CAM.13985

Li LX, Huang JJ, Han B, 2018. Centrifugal investigation of excavation adjacent to existing composite foundation. *Journal of Performance of Constructed Facilities*, 32(4): 04018044. https://doi.org/10.1061/(asce)cf.1943-5509.0001188

Li ZC, 2015. Deformation and Stability Investigation of Underground Excavations of Subway Transit System in Soft Clay. PhD Thesis, Zhejiang University, Hangzhou, China (in Chinese).

Li ZF, Lin WA, Ye JN, et al., 2021. Soil movement mechanism associated with arching effect in a multi-strutted excavation in soft clay. *Tunnelling and Underground Space Technology*, 110:103816. https://doi.org/10.1016/j.tust.2021.103816

Liang FY, Chu F, Song Z, et al., 2012. Centrifugal model test research on deformation behaviors of deep foundation pit adjacent to metro stations. *Rock and Soil Mechanics*, 33(3): 657-664 (in Chinese). https://doi.org/10.3969/j.issn.1000-7598.2012.03.003

Liao SM, Peng FL, Shen SL, 2008. Analysis of shearing effect on tunnel induced by load transfer along longitudinal direction. *Tunnelling and Underground Space Technology*, 23(4):421-430. https://doi.org/10.1016/j.tust.2007.07.001

Lim A, Ou CY, Hsieh PG, 2010. Evaluation of clay constitutive models for analysis of deep excavation under undrained conditions. *Journal of GeoEngineering*, 5(1):9-20. https://doi.org/10.6310/JOG.2010.5(1).2

Lim GT, 2004. Stabilisation of an Excavation by an Embedded Improved Soil Layer. PhD Thesis, National University of Singapore, Singapore.

Liu GB, Huang P, Shi JW, et al., 2016. Performance of a deep excavation and its effect on adjacent tunnels in Shanghai soft clay. *Journal of Performance of Constructed Facilities*, 30(6):04016041. https://doi.org/10.1061/(asce)cf.1943-5509.0000891

Liu SL, 2020. Centrifuge and Numerical Modeling of Long-Term Impacts of Excavation on Nearby Existing Tunnel in Soft Clayey Strata. PhD Thesis, Zhejiang University, Hangzhou, China (in Chinese).

Liu Y, Xiang BH, Fu MF, 2019. Observed performance of a large-scale deep triangular excavation in Shanghai soft clays. *Geotechnical and Geological Engineering*, 37(4): 2791-2809. https://doi.org/10.1007/s10706-018-00795-9

Meng FY, Chen RP, Liu SL, et al., 2021. Centrifuge modeling of ground and tunnel responses to nearby excavation in soft clay. *Journal of Geotechnical and Geoenvironmental Engineering*, 147(3):04020178. https://doi.org/10.1061/(asce)gt.1943-5606.0002473

Ng CWW, Hong Y, Liu GB, et al., 2012. Ground deformations and soil–structure interaction of a multi-propped excavation in Shanghai soft clays. *Géotechnique*, 62(10):907-921. https://doi.org/10.1680/geot.10.p.072

Ng CWW, Shi JW, Hong Y, 2013. Three-dimensional centrifuge modelling of basement excavation effects on an existing tunnel in dry sand. *Canadian Geotechnical Journal*, 50(8):874-888. https://doi.org/10.1139/cgj-2012-0423

Ng CWW, Sun HS, Lei GH, et al., 2015a. Ability of three different soil constitutive models to predict a tunnel's response to basement excavation. *Canadian Geotechnical Journal*,

52(11):1685-1698.
https://doi.org/10.1139/cgj-2014-0361

Ng CWW, Shi JW, Mašín D, et al., 2015b. Influence of sand density and retaining wall stiffness on three-dimensional responses of tunnel to basement excavation. *Canadian Geotechnical Journal*, 52(11):1811-1829.
https://doi.org/10.1139/cgj-2014-0150

Ou CY, Chiou DC, Wu TS, 1996. Three-dimensional finite element analysis of deep excavations. *Journal of Geotechnical Engineering*, 122(5):337-345.
https://doi.org/10.1061/(asce)0733-9410(1996)122:5(337)

Ou CY, Hsieh PG, 2011. A simplified method for predicting ground settlement profiles induced by excavation in soft clay. *Computers and Geotechnics*, 38(8):987-997.
https://doi.org/10.1016/j.compgeo.2011.06.008

Peng CY, Chen RP, Wang JF, et al., 2022. Field investigation into the performance of pipe pile in soft clay under static and cyclic axial loads. *Canadian Geotechnical Journal*, 59(8):1474-1486.
https://doi.org/10.1139/cgj-2021-0069

Plaxis BV, 2002. PLAXIS Finite Element Code for Soil and Rock Analyses. Seequent Limited, the Netherlands.

Purwana OA, 2006. Centrifuge Model Study on Spudcan Extraction in Soft Clay. PhD Thesis, National University of Singapore, Singapore.

Rampello S, Viggiani GMB, Amorosi A, 1997. Small-strain stiffness of reconstituted clay compressed along constant triaxial effective stress ratio paths. *Géotechnique*, 47(3): 475-489.
https://doi.org/10.1680/geot.1997.47.3.475

Ran L, Ding Y, Chen QZ, et al., 2023. Influence of adjacent shield tunneling construction on existing tunnel settlement: field monitoring and intelligent prediction. *Journal of Zhejiang University-SCIENCE A*, 24(12):1106-1119.
https://doi.org/10.1631/jzus.A2200573

Sagaseta C, 1987. Analysis of undrained soil deformation due to ground loss. *Géotechnique*, 37(3):301-320.
https://doi.org/10.1680/geot.1987.37.3.301

Schofield AN, 1980. Cambridge geotechnical centrifuge operations. *Géotechnique*, 30(3):227-268.
https://doi.org/10.1680/geot.1980.30.3.227

Sharma JS, Hefny AM, Zhao J, et al., 2001. Effect of large excavation on deformation of adjacent MRT tunnels. *Tunnelling and Underground Space Technology*, 16(2):93-98.
https://doi.org/10.1016/s0886-7798(01)00033-5

Shi CH, Cao CY, Lei MF, et al., 2016. Effects of lateral unloading on the mechanical and deformation performance of shield tunnel segment joints. *Tunnelling and Underground Space Technology*, 51:175-188.
https://doi.org/10.1016/j.tust.2015.10.033

Shi JW, 2015. Investigation of Three-Dimensional Tunnel Responses due to Basement Excavation. PhD Thesis, Hong Kong University of Science and Technology, Hong Kong, China.

Shi JW, Liu GB, Huang P, et al., 2015a. Interaction between a large-scale triangular excavation and adjacent structures in Shanghai soft clay. *Tunnelling and Underground Space Technology*, 50:282-295.
https://doi.org/10.1016/j.tust.2015.07.013

Shi JW, Ng CWW, Chen YH, 2015b. Three-dimensional numerical parametric study of the influence of basement excavation on existing tunnel. *Computers and Geotechnics*, 63:146-158.
https://doi.org/10.1016/j.compgeo.2014.09.002

Shi JW, Ng CWW, Chen YH, 2017. A simplified method to estimate three-dimensional tunnel responses to basement excavation. *Tunnelling and Underground Space Technology*, 62:53-63.
https://doi.org/10.1016/j.tust.2016.11.007

Shi JW, Ding C, Ng CWW, et al., 2020. Effects of overconsolidation ratio on tunnel responses due to overlying basement excavation in clay. *Tunnelling and Underground Space Technology*, 97:103247.
https://doi.org/10.1016/j.tust.2019.103247

Shibuya S, Hwang SC, Mitachi T, 1997. Elastic shear modulus of soft clays from shear wave velocity measurement. *Géotechnique*, 47(3):593-601.
https://doi.org/10.1680/geot.1997.47.3.593

Sun YH, Wang HL, Meng FY, et al., 2025. Multiscale mechanical behaviour of sand–steel structure interface for deep underground space. *Canadian Geotechnical Journal*, 62: 1-16.
https://doi.org/10.1139/cgj-2025-0026

Tan Y, Wei B, 2012. Observed behaviors of a long and deep excavation constructed by cut-and-cover technique in Shanghai soft clay. *Journal of Geotechnical and Geoenvironmental Engineering*, 138(1):69-88.
https://doi.org/10.1061/(asce)gt.1943-5606.0000553

Taylor RN, 2018. Geotechnical Centrifuge Technology. CRC Press, London, UK.
https://doi.org/10.1201/9781482269321

Wang HL, Yin ZY, 2020. High performance prediction of soil compaction parameters using multi expression programming. *Engineering Geology*, 276:105758.
https://doi.org/10.1016/j.enggeo.2020.105758

Wang HL, Cui YJ, Lamas-Lopez F, et al., 2018. Permanent deformation of track-bed materials at various inclusion contents under large number of loading cycles. *Journal of Geotechnical and Geoenvironmental Engineering*, 144(8): 04018044.
https://doi.org/10.1061/(asce)gt.1943-5606.0001911

Wang HL, Sun YH, Chen RP, et al., 2024. Deformation characteristics and stability analysis of lean clay under cyclic loading. *Transportation Geotechnics*, 47:101285.
https://doi.org/10.1016/j.trgeo.2024.101285

Wang WD, Wang HR, Xu ZH, 2013. Study of parameters of HS-Small model used in numerical analysis of excavations in Shanghai area. *Rock and Soil Mechanics*, 34(6): 1766-1774 (in Chinese).
https://doi.org/10.16285/j.rsm.2013.06.022

Xie Y, Leung CF, Chow YK, 2012. Centrifuge modelling of spudcan–pile interaction in soft clay. *Géotechnique*, 62(9): 799-810.
https://doi.org/10.1680/geot.12.og.003

Zhang DM, Xie XC, Li ZL, et al., 2020. Simplified analysis method for predicting the influence of deep excavation on existing tunnels. *Computers and Geotechnics*, 121:103477. https://doi.org/10.1016/j.compgeo.2020.103477

Zhang XH, Zhai ZJ, Wang HL, et al., 2025. A deformation-dependent model for passive soil arching in sand. *Acta Geotechnica*, in press. https://doi.org/10.1007/s11440-025-02733-5

Zhang ZG, Zhang MX, Zhao QH, 2015. A simplified analysis for deformation behavior of buried pipelines considering disturbance effects of underground excavation in soft clays. *Arabian Journal of Geosciences*, 8(10):7771-7785. https://doi.org/10.1007/s12517-014-1773-4

Zheng G, Wei SW, Peng SY, et al., 2010. Centrifuge modeling of the influence of basement excavation on existing tunnels. *In*: Springman S, Laue J, Seward L (Eds.), Physical Modelling in Geotechnics, Two Volume Set. CRC Press, London, UK, p.523-527. https://doi.org/10.1201/b10554-88

Zheng G, Du YM, Cheng X, et al., 2017. Characteristics and prediction methods for tunnel deformations induced by excavations. *Geomechanics and Engineering*, 12(3):361-397. https://doi.org/10.12989/gae.2017.12.3.361